Planar waveguides with less than 0.1 dB/m propagation loss fabricated with wafer bonding

Jared F. Bauters,[1,*] Martijn J. R. Heck,[1] Demis D. John,[1] Jonathon S. Barton,[1] Christiaan M. Bruinink,[2] Arne Leinse,[2] René G. Heideman,[2] Daniel J. Blumenthal,[1] and John E. Bowers[1]

[1]*Department of Electrical and Computer Engineering, University of California, Santa Barbara, CA 93106, USA*
[2]*LioniX BV, P.O. Box 456, 7500 AH, Enschede, the Netherlands*
[*]jbauters@ece.ucsb.edu

Abstract: We demonstrate a wafer-bonded silica-on-silicon planar waveguide platform with record low total propagation loss of (0.045 ± 0.04) dB/m near the free space wavelength of 1580 nm. Using coherent optical frequency domain reflectometry, we characterize the group index, fiber-to-chip coupling loss, critical bend radius, and propagation loss of these waveguides.

©2011 Optical Society of America

OCIS codes: (130.0130) Integrated Optics; (230.7390) Waveguides, planar.

References and links

1. C. Ciminelli, F. Dell'Olio, C. E. Campanella, and M. N. Armenise, "Photonic technologies for angular velocity sensing," Adv. Opt. Photon. **2**(3), 370–404 (2010).
2. K. Horikawa, I. Ogawa, T. Kitoh, and H. Ogawa, "Silica-based integrated planar lightwave true-time-delay network for microwave antenna applications," in *Proceedings of the Optical Fiber Communication Conference*, (San Jose, Calif., 1996), Vol. 2, pp. 100–101.
3. E. F. Burmeister, D. J. Blumenthal, and J. E. Bowers, "A comparison of optical buffering technologies," Opt. Switching Networking **5**(1), 10–18 (2008).
4. M.-C. Tien, J. F. Bauters, M. J. R. Heck, D. T. Spencer, D. J. Blumenthal, and J. E. Bowers, "Ultra-high quality factor planar Si_3N_4 ring resonators on Si substrates," Opt. Express **19**(14), 13551–13556 (2011).
5. D. D. John, J. F. Bauters, J. Nedy, W. Li, R. Moreira, J. S. Barton, J. E. Bowers, and D. J. Blumenthal, "Fabrication and Demonstration of a Pure Silica-Core Waveguide Utilizing a Density-Based Index Contrast," in *Proceedings of OFC* (Los Angeles, CA, 2011).
6. T. J. Kippenberg, S. M. Spillane, and K. J. Vahala, "Demonstration of ultra-high-Q small mode volume toroid microcavities on a chip," Appl. Phys. Lett. **85**(25), 6113–6115 (2004).
7. K. P. Jackson, S. A. Newton, B. Moslehi, M. Tur, C. C. Cutler, J. W. Goodman, and H. J. Shaw, "Optical fiber delay-line signal processing," IEEE Trans. Microw. Theory Tech. **33**(3), 193–210 (1985).
8. Y. Li and C. Henry, "Silica-based optical integrated circuits," IEE Proc., Optoelectron. **143**(5), 263 (1996).
9. R. Adar, M. Serbin, and V. Mizrahi, "Less than 1 dB per meter propagation loss of silica waveguides measured using a ring resonator," J. Lightwave Technol. **12**(8), 1369–1372 (1994).
10. T. Kominato, Y. Hida, M. Itoh, H. Takahashi, S. Sohma, T. Kitoh, and Y. Hibino, "Extremely low-loss (0.3 dB/m) and long silica-based waveguides with large width and clothoid curve connection," in *Proceedings of ECOC* (Stockholm, Sweden, 2004).
11. J. F. Bauters, M. J. R. Heck, D. D. John, M.-C. Tien, J. S. Barton, D. J. Blumenthal, and J. E. Bowers, "Low Loss Planar Waveguides," in *Proceedings of ECOC* (Geneva, Switzerland, 2011).
12. J. F. Bauters, M. J. R. Heck, D. John, D. Dai, M. C. Tien, J. S. Barton, A. Leinse, R. G. Heideman, D. J. Blumenthal, and J. E. Bowers, "Ultra-low-loss high-aspect-ratio Si_3N_4 waveguides," Opt. Express **19**(4), 3163–3174 (2011).
13. D. Dai, J. F. Bauters, M. Tien, M. Heck, D. Blumenthal, and J. E. Bowers, "Polarization characteristics of low-loss nano-core buried optical waveguides and directional couplers," in *Proceedings of GFP* (Beijing, China, 2010).
14. D. Dai, Z. Wang, J. F. Bauters, M.-C. Tien, M. J. R. Heck, D. J. Blumenthal, and J. E. Bowers, "Low-loss Si_3N_4 arrayed-waveguide grating (de)multiplexer using nano-core optical waveguides," Opt. Express **19**(15), 14130–14136 (2011).
15. F. Ay and A. Aydinli, "Comparative investigation of hydrogen bonding in silicon based PECVD grown dielectrics for optical waveguides," Opt. Mater. **26**(1), 33–46 (2004).
16. P. Bienstman, S. Selleri, L. Rosa, H. P. Uranus, W. C. L. Hopman, R. Costa, A. Melloni, L. C. Andreani, J. P. Hugonin, P. Lalanne, D. Pinto, S. S. A. Obayya, M. Dems, and K. Panajotov, "Modeling leaky photonic wires: A mode solver comparison," Opt. Quantum Electron. **38**(9-11), 731–759 (2007).
17. L. U. J. T. Ogbuji and S. Bryan, "The SiO_2-Si_3N_4 Interface, Part I: Nature of the Interphase," J. Am. Ceram. Soc. **78**(5), 1272–1278 (1995).

18. W. D. Callister and D. G. Rethwisch, *Materials Science and Engineering: An Introduction* (Wiley, 2010).
19. A. del Prado, E. San Andrés, F. L. Martínez, I. Mártil, G. González-Díaz, W. Bohne, J. Rohrich, B. Selle, and M. Fernández, "Composition and optical properties of silicon oxynitride films deposited by electron cyclotron resonance," Vacuum **67**(3-4), 507–512 (2002).
20. B. J. Soller, D. K. Gifford, M. S. Wolfe, and M. E. Froggatt, "High resolution optical frequency domain reflectometry for characterization of components and assemblies," Opt. Express **13**(2), 666–674 (2005).
21. U. Glombitza and E. Brinkmeyer, "Coherent Frequency-Domain Reflectometry for Characterization of Single-Mode Integrated-Optical Waveguides," J. Lightwave Technol. **11**(8), 1377–1384 (1993).
22. M. Stadtmüeller, "Mechanical Stress of CVD-Dielectrics," J. Electrochem. Soc. **139**(12), 3669–3674 (1992).
23. E. P. EerNisse, "Stress in thermal SiO₂ during growth," Appl. Phys. Lett. **35**(1), 8–10 (1979).
24. L. A. Coldren and S. W. Corzine, *Diode Lasers and Photonic Integrated Circuits*, 337 (Wiley, 1995).

1. Introduction

Planar waveguides with ultra-low propagation loss are necessary for the long propagation distances and high quality factor resonators used in photonic rotational velocity sensors [1], true-time-delay networks [2], optical buffers [3], and narrowband photonic filters [4]. The history of optical fiber loss reduction suggests that a large modal overlap with undoped silica is a path to ultra-low propagation loss [5]. Indeed, the high optical quality of thermally grown silicon dioxide has been used in the fabrication of ultra-high-Q microtoroid resonators-on-a-chip with intrinsic quality factors greater than 400 million [6]. However, resonator structures are unsuitable for many high performance optical gyroscope and delay line designs [1,7]. Also, tapered fiber couplers are typically used to couple light into microtoroid resonators, making them difficult to integrate with other photonic components for increased functionality. Therefore, an ultra-low-loss *planar* waveguide platform that is suitable for resonator structures, spiral delays, and photonic integration is still needed.

In most silica-based planar waveguide platforms, the optical mode is highly confined to a low-index-contrast core that is several microns in width and height [8–10]. With core confinement factors greater than 70% calculated for an index contrast of 0.7% and a free-space wavelength of 1550 nm, the quality of the core material is emphasized in these structures. Since the cladding material is typically SiO₂, the small refractive index contrast is created through the deposition of doped SiO₂ cores [8–10]. Adar *et al*. reported the lowest single-mode propagation loss to date, 0.85 dB/m, using such a design with phosphorus-doped cores deposited through plasma-enhanced chemical vapor deposition (PECVD) [9]. Using a larger, multimode core design, Kominato *et al*. reported 0.3 dB/m propagation loss for germanium-doped cores deposited with flame hydrolysis [10].

Recently, we demonstrated record low 0.7 dB/m single-mode propagation loss for the TE mode in planar silica-on-silicon spiral waveguide delays [11]. Due to the thin core geometry in these structures, the core confinement factor was about 3%, and a majority of the optical mode propagated in the silicon dioxide cladding layers. The large effective mode area that resulted from the high-aspect-ratio core geometry of our waveguides, calculated to be around $5\ \mu m^2$ at a free-space wavelength of 1550 nm, and a photoresist reflow process contributed to the reduction of interfacial scattering loss. Additional photonic components, including ultra-high-Q ring resonators, multi-mode interferometers, polarizers, Mach-Zehnder interferometers, and arrayed-waveguide gratings have been demonstrated with this planar waveguide platform [4,11–14].

Though the overlap with SiO₂ cladding layers was around 97% for the waveguides reported in [11], the upper cladding was deposited with silane and nitrous oxide-based plasma-enhanced chemical vapor deposition (PECVD). It is well known that impurity hydrogen atoms incorporated into silica films bond with nitrogen, silicon, and oxygen atoms, resulting in overtone absorption losses [15]. Furthermore, we expect such losses to be highest in PECVD layers deposited at low temperatures. In this paper, we report a wafer-bonded upper cladding structure that is designed to increase the modal overlap with high quality, *thermally grown* silicon dioxide layers. Using this structure, we demonstrate record low propagation loss in a planar waveguide spiral delay. We begin with a description of the waveguide fabrication process. We then compare coherent optical frequency domain reflectometry (OFDR) characterization results from spiral waveguide delays fabricated with

PECVD and wafer-bonded thermal oxide upper claddings. Group index, coupling loss, critical bend radius, and propagation loss are reported.
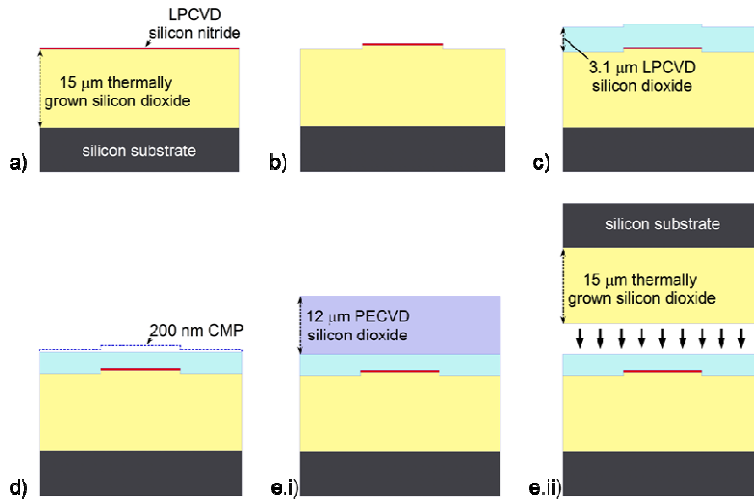
2. Waveguide fabrication

Fig. 1. A schematic overview of the processes used to fabricate the waveguides discussed in this paper. e.i and e.ii illustrate the two upper cladding approaches.

Waveguide fabrication begins with a silicon substrate and 15 microns of thermally grown silicon dioxide lower cladding. The thickness is chosen to limit the theoretical substrate leakage loss of the fundamental TE mode to less than 0.01 dB/m for the waveguides in this work [16]. Low-pressure chemical vapor deposition (LPCVD) is then used to deposit either a 50 or a 40-nm-thick stoichiometric Si_3N_4 film, giving a fixed index contrast of around 23% (n_{core} = 1.98 to n_{clad} = 1.45) with the silicon dioxide layers (Fig. 1a). Contact lithography is performed, and the developed photoresist is then reflowed on a hotplate in order to reduce the line edge roughness before etching. Reactive ion etching is used to etch through the Si_3N_4 film, thus defining the waveguide core widths (Fig. 1b). In this work, the nominal core widths range from 2.15 to 15 microns on the lithography mask plate.

Three 1.1-¯m-thick SiO_2 layers are then deposited using tetraethylorthosilicate (TEOS)-based LPCVD. A three hour 1150 °C anneal is performed after the deposition of each layer, giving a TEOS layer thickness of 3.1 microns (Fig. 1c). The resulting protrusion of SiO_2 above the waveguide cores is removed through chemical mechanical polishing, which consumes altogether 200 nm of the TEOS layer (Fig. 1d). After polishing, the waveguide upper cladding is completed through either PECVD or wafer-bonding processes. In the former (Fig. 1e.i), PECVD is used to deposit 12 microns of SiO_2, and the finished wafer is annealed for an additional 3 hours at 1150 °C. In the latter process (Fig. 1e.ii), an additional silicon substrate with 15 microns of thermally grown silicon dioxide and the unfinished waveguide wafer are treated with O_2 plasma and brought into contact before spontaneous bonding at room temperature and pressure. To strengthen the bond, the wafer couple is annealed at 950 °C for 3 hours. Since the 15 ¯m thermal oxide wafers are available at the start of waveguide processing, the wafer-bonding process is faster than the PECVD deposition process. Data in the following sections also suggests that the wafer-bonding process introduces less stress in the dielectric films. A large amount of film stress can cause manufacturing problems, such as wafer cracking during handling and dicing, as well as waveguide design problems due to the perturbation in film refractive indices caused by the stress-optical effect.

Due to the high temperature anneal steps in the above processes, the core and cladding materials interdiffuse at the upper, lower, and sidewall interfaces. In [17], Auger electron spectroscopy (AES) measurements performed on Si_3N_4-SiO_2 diffusion couples reveal the

formation of a "graded suboxide" between the Si_3N_4 and SiO_2 layers during high temperature anneals. The dependence of this middle oxynitride's composition on distance from the Si_3N_4-SiO_2 interface fits well to the analytic solution of Fick's second law for the diffusion of a semi-infinite material whose initial concentration profile can be described with a Heaviside step function [18]. This solution is

$$C\big(D(T),x,t\big) = \frac{(c_1+c_2)}{2} - \frac{(c_1-c_2)}{2} erf\left(\frac{x}{2\sqrt{D(T)t}}\right) \qquad (1)$$

where c_1 is the greater concentration in the step function, c_2 is the lesser concentration, $D(T)$ is the temperature dependent diffusivity, x is the distance from the Si_3N_4-SiO_2 interface, and t is time. Nonlinear fits of Eq. (1) to data taken at 1200 and 1350 °C in [17] are used to estimate D(1200) and D(1350) as 0.03 and 0.39 nm^2/s, respectively. D(T) is then assumed to follow an Arrhenius relation, such that an estimate of the interdiffused composition of our waveguide interfaces can be obtained using Eq. (1) with D(1150) ~0.01 nm^2/s. Assuming a linear dependence of refractive index on the mole fraction of Si_3N_4 and SiO_2 in the graded oxynitride region as measured in [19], the estimated refractive index profiles at the core-cladding interfaces of our waveguides are shown in Fig. 2a. Since the graded region extends about 10 nm into the core at each interface and the thinnest waveguide cores are around 40 nm thick, the assumption of a semi-infinite material in the above calculation is valid. An SEM micrograph of a cleaved waveguide facet with a nominally 40-nm-thick core is shown in Fig. 2b. An actual core deposition thickness of 39.4 nm is measured with ellipsometry on a sample that is not annealed. The inset to Fig. 2b is an SEM image of the same waveguide core, taken at a higher magnification. Using this image, a core thickness of ~35 nm is measured, supporting our estimate of an effectively thinner core due to interdiffusion of the core and cladding materials. This reduced thickness also agrees with the bend loss data given below.
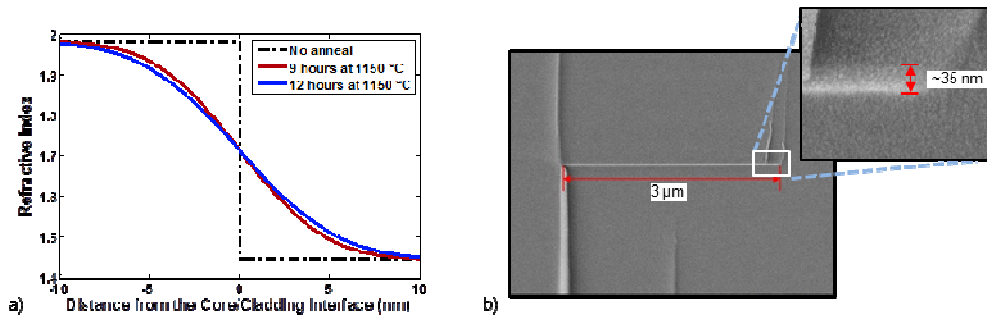

Fig. 2. a) Calculated refractive index profile of an interdiffused core/cladding interface and b) an SEM micrograph of a waveguide core. The inset shows a high magnification SEM of the region outlined in white. The value shown is the average of many measurements taken along the core The standard deviation of those measurements is 2 nm.

3. Waveguide characterization

Reflectometry is widely used in fiber optics to probe the local reflectivity of waveguides and devices with respect to propagation distance [20]. With a point-to-point resolution of about 10 ¯m and a detection sensitivity of −130 dB over 30 meters of propagation, *coherent optical frequency domain reflectometry* (OFDR) is a particularly useful technique for characterizing waveguides and devices at the planar scale [12, 21]. In OFDR, a continuous wave laser source is scanned over several terahertz in frequency or, equivalently, several tens of nanometers in wavelength. A larger scan range improves the spatial resolution of the measurement according to

$$D_{\min} \cong \frac{c}{2n_g \left| f_{start} - f_{end} \right|} = \frac{\lambda_{start} \lambda_{end}}{2n_g \left| \lambda_{start} - \lambda_{end} \right|} \qquad (2)$$

where $D_{\min}$ is the minimum distance between two data points, c is the speed of light, n_g is the group index, f_{start} and λ_{start} are the source frequency and wavelength at the start of the scan, and f_{end} and λ_{end} are the source frequency and wavelength at the end of the scan [20]. All parameters derived from the spatial domain data, however, are then averages over the spectral range of the measurement scan. If the spectral dependence of a parameter is desired, a rectangular window function can be applied to data in the spectral domain in order to narrow the included spectral range. This window can be moved across the full spectral range of the measurement, allowing one to extract the parameter at each window position, obtaining the spectral dependence of a parameter from a single OFDR scan. Since narrowing the data in the frequency domain decreases the spatial resolution of the measurement according to Eq. (2), there is a tradeoff between spectral averaging, which can distort the actual spectral dependence, and measurement accuracy. In this work, a window width of 10 nm is used to extract spectrally dependent measurements of group index, coupling loss, critical bend radius, and propagation loss.

3.1 Group index

In OFDR, data are collected as the frequency of a laser source is swept, giving what are commonly called the "frequency domain" data [20]. The reflectivity of the waveguide or device with respect to group delay is then obtained from a discrete Fourier transform of these data. In order to transform the group delay domain data to the spatial domain, the group delay domain must be scaled by the factor $\left(c/n_g \right)$, where c is the speed of light in vacuum and n_g is the group index of the mode propagating in the structure. An approximate n_g is typically assumed during an OFDR measurement, allowing immediate feedback in the more intuitive spatial domain. However, one can measure n_g using OFDR by comparing the measured distance between two reflection events to the actual distance. The measured group index, n_g, is then obtained from the assumed group index, $n_g^{assumed}$, by

$$n_g = \left(\frac{D^{measured}}{D^{actual}} \right) n_g^{assumed} \qquad (3)$$

where $D^{measured}$ and D^{actual} are the measured and actual distances between the two reflections, respectively. Given uncertainties in the measured distance, $D^{measured} = D_0^{measured} + \Delta D^{measured}$, and the actual distance, $D^{actual} = D_0^{actual} + \Delta D^{actual}$, between the two reflections, the uncertainty in the measured group index, Δn_g, can be estimated as

$$
\begin{aligned}
\Delta n_g &= \left(\frac{\partial n_g}{\partial D^{measured}} \right) \Delta D^{measured} + \left(\frac{\partial n_g}{\partial D^{actual}} \right) \Delta D^{actual} \\
&\cong \left(\frac{1}{D^{actual}} \right) \left(\frac{\pm c}{2 \left| f_{start} - f_{end} \right|} - n_g \Delta D^{actual} \right)
\end{aligned}
\qquad (4)
$$

where we have used Eq. (2) to approximate $\Delta D^{measured}$ as $\pm D_{\min}$, and we assume $n_g^{assumed} / n_g \cong 1$. The inverse relationship between Δn_g and $\left| f_{start} - f_{end} \right|$ in Eq. (4) illustrates the tradeoff between parameter uncertainty and spectral averaging.

Figure 3a shows reflection amplitude data measured for a waveguide spiral delay consisting of cores that are 40 nm thick and 6.0 ¯m wide. The data have a 10 nm window centered at 1600 nm applied in the spectral domain, and the upper cladding of the waveguide is bonded thermal oxide. An initial value of 1.5 is used for $n_g^{assumed}$. Using the distance measured between reflections at the input and output facets of this spiral delay as $D^{measured}$ and the length of the spiral delay on the lithographic mask plate, 1.032232 m, as D^{actual} , n_g of the propagating mode is determined using Eq. (3) to be 1.4815. The uncertainty in the length of the spiraled waveguide, ΔD^{actual} , has differing upper and lower bounds. The upper bound is given by lithographic errors that could possibly add length to the mask plate value. The lower bound is due to a possible misalignment of the dicing blade, which could remove length from the mask plate value. We assume the effect on Δn_g due to lithographic errors to be negligible such that the lower bound on Δn_g is dominated by the first term in Eq. (4). We include both terms in the upper bound on Δn_g , using a value for ΔD^{actual} equal to twice the approximate kerf width of our dicing blade, or 200 ¯m. The upper and lower bounds on Δn_g are then calculated to be 5.3×10^{-4} and -2.4×10^{-4}, respectively, for our measurements.
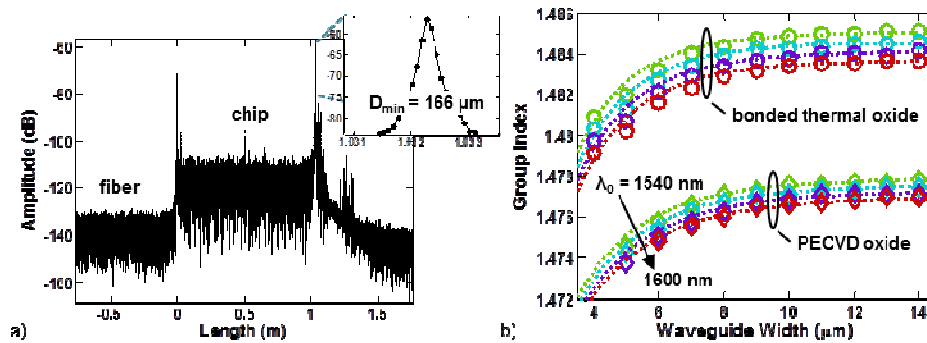

Fig. 3. a) OFDR data from a 40-nm-thick waveguide with a 10 nm window function centered at 1600 nm applied in the spectral domain. The inset, a blown up section of the data, shows the uncertainty of 166 ¯m in facet position. b) Group index vs. waveguide width for a range of wavelengths. Waveguide cores are nominally 40-nm-thick with bonded thermal oxide (circles) and PECVD oxide (diamonds) upper claddings. Dashed lines are simulated.

Figure 3b shows the group indices measured for waveguides with 40-nm-thick cores, various core widths, and bonded thermal (circle) or PECVD oxide (diamond) upper claddings. All measurements are taken with a 10 nm window applied in the spectral domain, and data are shown for windows centered at 1540, 1560, 1580, and 1600 nm. A significant offset exists between data measured from waveguides with bonded thermal and PECVD oxide upper claddings. The offset is an order of magnitude larger than the bounds on Δn_g and must therefore be due to a physical difference between the waveguides. Though waveguides with PECVD and bonded thermal oxide upper claddings underwent different total anneal times of 12 and 9 hours at 1150 °C, the resulting calculated refractive index profiles shown in Fig. 2a do not account for the entire offset between the measured group indices. Dielectric film stress causes a shift in refractive index according to the stress-optical effect. Different film stresses could make up the rest of the offset since deposited and thermally grown oxides have distinct intrinsic stress contributions, and the different total anneal times result in differing amounts of thermal stress [22, 23]. The dashed lines in Fig. 3b indicate group indices simulated in Photon Design's FIMMWAVE mode solver using uniform core and cladding refractive indices. Core/cladding indices of 1.96/1.4658 and 1.87/1.4656 give good fits to the data taken from waveguides with bonded thermal and PECVD oxide upper claddings, respectively. So in

conclusion, we measure different group velocities for the fundamental TE modes in waveguides with bonded thermal and PECVD oxide upper claddings, and we attribute this offset to differences in core/cladding interdiffusion and dielectric film stress between the two processes.
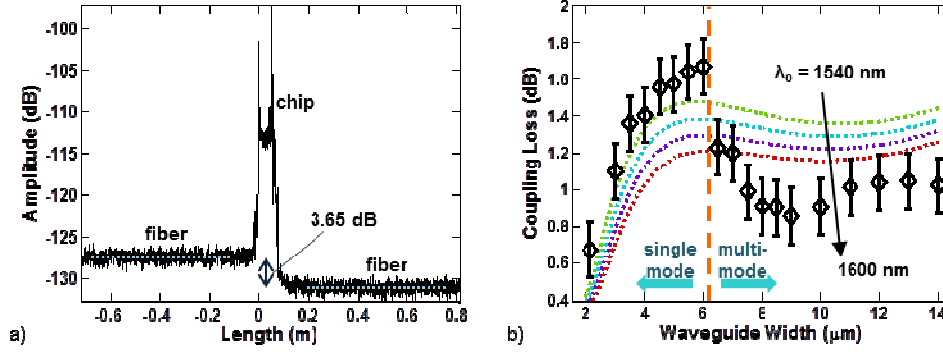
3.2 Fiber-to-chip coupling loss

Fig. 4. a) OFDR backscatter data from a 50-nm-thick waveguide coupled to cleaved SMF-28 fibers with index matching gel (n = 1.46). b) Coupling loss vs. waveguide width. Waveguide cores are nominally 50-nm-thick with PECVD oxide upper cladding. Dashed lines are simulated over a range of wavelengths.

Figure 4a shows OFDR data from two cleaved SMF-28 fibers coupled to a waveguide s-bend with index matching gel. The s-bend is 54 mm long with a bend radius of 27 mm. The waveguide has PECVD oxide upper cladding and a core that is 50-nm-thick by 10-¯m-wide. The data is not filtered in the spectral domain, but a moving average filter with a 100-data-point or ~1 mm window size is applied in the spatial domain in order to reduce the backscatter amplitude deviation. Before the OFDR scan, the fiber-to-chip coupling is maximized using the OFDR source laser, a 3-paddle polarizer, and an optical power meter. The dashed lines in the figure indicate the mean backscatter levels from the input and output coupling fibers. The difference between these two levels, 3.65 dB, is made up of the total return loss occurring between the two fibers, or

$$RL_{dB}^{total} = 2IL_{dB}^{total} = 2\left(IL_{dB}^{fiber-to-chip} + IL_{dB}^{propagation} + IL_{dB}^{fiber-to-chip} \right) \qquad (5)$$

where RL_{dB}^{total} is the total return loss in dB, IL_{dB}^{total} is the total insertion loss, $IL_{dB}^{fiber-to-chip}$ is the fiber-to-chip insertion loss per facet, and $IL_{dB}^{propagation}$ is the total propagation insertion loss. For this case, $IL_{dB}^{propagation}$ is 0.01 dB, giving a fiber-to-chip coupling loss of 0.91 dB per facet.

The markers in Fig. 4b are coupling loss data for a range of waveguide core widths from the same wafer. The dashed lines in the figure are simulated coupling losses between a fiber-like Gaussian beam and the fundamental TE modes of the planar waveguides. The Gaussian beam is perfectly collimated and TE-polarized with a spot diameter of 10.4 ¯m. The losses are simulated with Photon Design's FIMMPROP software with the beam impinging from a uniform refractive index of 1.6 in order to account for the index matching gel. The majority of the coupling loss is due to the mismatch in shape between the fiber and planar waveguide modes. For the narrowest core widths shown, the planar waveguide mode has its lowest horizontal and vertical confinement and is best matched to the fiber mode. The coupling loss is therefore minimal in this regime, and this allows for the fabrication of low-loss spot size converters through the tapering of waveguide core width to around 2 ¯m. The coupling loss then increases with increasing core width as the confinement of the fundamental TE mode increases. As the core width increases beyond the point of minimum horizontal mode diameter (see Fig. 4 in [12] for a visualization), however, the planar waveguide mode size

again becomes more closely matched to the fiber spot diameter. Coupling loss then reaches a local minimum in the 9-10 ̄m core width regime. The large decrease in coupling loss from the 6 to the 7 ̄m wide core, which disagrees with the simulation, is possibly due to increased confinement of the fundamental TM mode along with insufficient TM mode extinction. The decrease may also be due to increased confinement of the second order TE mode along with a horizontal misalignment of the coupling fibers.

3.3 Critical bend radius

Figure 5 shows red light propagating in a spiraled waveguide structure designed for OFDR characterization of bend radiation loss. Though the spiral consists of a waveguide bus with 12 different core widths ranging from 3 to 14 ̄m, each waveguide begins with a single-mode core width of 5 ̄m for the first 150 ̄m of propagation. The core is then linearly tapered out to the final width over the next 22 mm. The long, adiabatic taper ensures an efficient launch of only the fundamental mode in the wider, multimode waveguide cores. The waveguides in the bus have a center-to-center spacing of 50 ̄m in order to prevent crosstalk that could influence the measurement. An Archimedean spiral design is used such that the bend radius of each waveguide in the bus decreases linearly and by the same amount over each round-trip. This results in the nonlinear relationship between bend radius and propagation length shown in the inset to Fig. 5, or

$$r(z) = \sqrt{b^2 + (s/\pi)z} \tag{6}$$

where r is the bend radius, z is propagation length, b is the starting radius, and s is the change in bend radius per round trip.
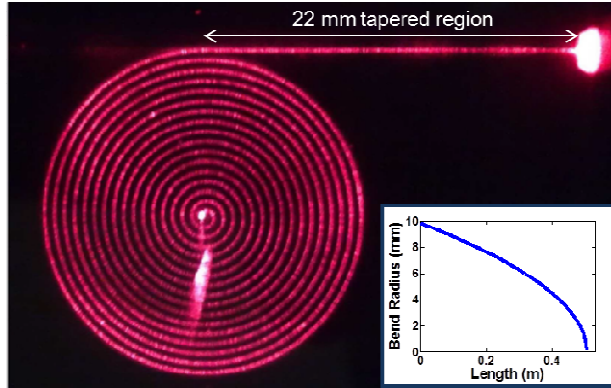

Fig. 5. Red laser light propagating in a waveguide that spirals from a bend radius of around 10 mm down to a bend radius of around 165 ̄m. The inset shows the exact dependence of bend radius on propagation length.

Figure 6a shows OFDR data from a 40-nm-thick by 5.0- ̄m-wide waveguide with bonded thermal oxide upper cladding. The data are filtered in the spectral domain with a 10 nm window centered at 1550 nm. The solid line is a nonlinear fit to the OFDR data of

$$\begin{aligned} R_{dB}(z) &= 10\log\left[\exp\left\{-2(\alpha_1 + \alpha_2(z))z\right\}\right] + R_{offset} \\ &= -20\log(e)[\alpha_1 + \alpha_2(z)]z + R_{offset} \end{aligned} \tag{7}$$

where R_{dB} is the OFDR reflectivity amplitude, z is propagation length, α_1 is a propagation loss constant, α_2 is a propagation loss coefficient that depends on propagation length, and R_{offset} is equal to the backscatter level of the waveguide minus any loss that takes place before the beginning of the fit region, such as the fiber-to-chip coupling loss. The propagation loss

constant, α_1, in Eq. (7) includes the scattering and impurity overtone absorption losses in the waveguide, which are assumed to not greatly differ with waveguide bend radius. The length dependent propagation coefficient, α_2, represents bend radiation loss, which theoretically has an exponential dependence on bend radius [24], or

$$\alpha_2(z) = a_1 e^{-a_2 r(z)} \qquad (8)$$

where a_1 and a_2 are constants of the exponential fit, and $r(z)$ is given in Eq. (6). The fit for a_1 and a_2 allows one to determine the bending capabilities of the waveguide.
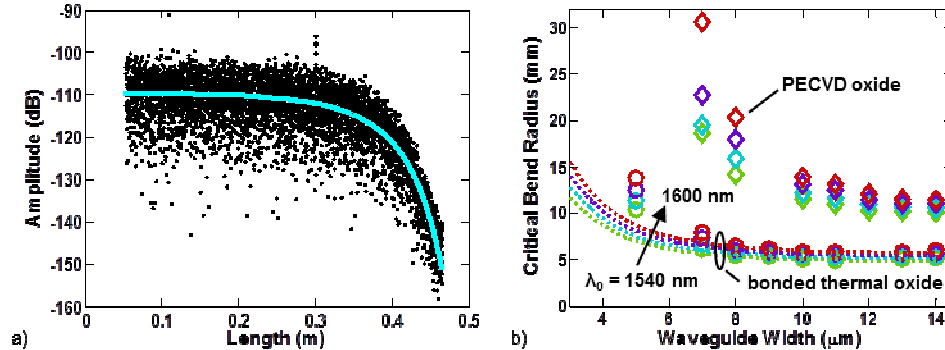
Fig. 6. a) OFDR data from a 40-nm-thick by 5.0-¯m-wide waveguide with a 10 nm window function centered at 1550 nm applied in the spectral domain. The solid line is a nonlinear fit of Eq. (7) to the data. b) Critical bend radius (radius at which bend loss = 0.1 dB/m) vs. waveguide width for a range of wavelengths. Waveguide cores are nominally 40-nm-thick with bonded thermal oxide (circles) and PECVD oxide (diamonds) upper claddings. Dashed lines are simulated values.

Figure 6b shows the results of such nonlinear fitting to OFDR data measured from waveguides with 40-nm-thick cores, various core widths, and PECVD (diamond) or bonded thermal (circle) oxide upper claddings. In this paper, the critical bend radius is defined as the radius at which bend loss is equal to 0.1 dB/m. The data follow an expected trend where the critical bend radius decreases as core width and modal confinement increase. Confinement increases by only a small amount, however, as the waveguide core width exceeds its maximum single-mode value, such that little is gained in critical bend radius beyond that width. There is, again, an offset between data measured from waveguides with PECVD and bonded thermal oxide upper claddings. As for the group index data, this offset can be attributed to core/cladding interdiffusion and stress-optical effects. The larger critical bend radii for the waveguides with PECVD oxide upper cladding agree well with the fit refractive indices from Section 3.1, which indicate a lower index contrast for the PECVD waveguides compared to those with bonded thermal oxide upper cladding. The dashed lines in Fig. 6b are simulated using a staircase approximation to the continuous refractive index profile shown in Fig. 2a across the top and bottom interfaces. A conformal transformation is used along with perfectly matched layers to obtain the loss due to bend radiation as in [12]. The uncertainty in group index, Δn_g, calculated in Section 3.1 can be carried over to these fits to yield an uncertainty in critical bend radius of around 0.1 mm. So in conclusion, we see an offset in the bending capabilities of waveguides fabricated with bonded thermal and PECVD oxide upper claddings. The offset agrees with the analysis of an offset in group index data shown in Section 3.1, and this suggests different core/cladding interdiffusion and dielectric film stress between the two processes.

3.4 Propagation loss

Figure 3a shows OFDR data that can be used to measure the group index of the fundamental TE mode propagating in the 1.032 meters of planar waveguide. After measuring the group index, the same spiral delay structure can be used along with Eq. (7) to determine the propagation loss of the mode. If one avoids regions of significant bend loss, the length dependent loss coefficient can be ignored such that a simpler linear fit may be used

$$R_{dB}(z) = 2\alpha_1^{dB/m} z + R_{offset}^{dB/m} \tag{9}$$

where $2\alpha_1^{dB/m}$ is the return loss in dB/m due to propagation (the slope of the OFDR reflectivity data with respect to propagation length), and $R_{offset}^{dB/m}$ is the vertical axis offset of the fit line. The spiral delay used in this measurement, shown in Fig. 7 with red light injected, consists of a waveguide bus with 20 core widths ranging from 2.15 to 14.0 ¯m. Linear tapers are used, as in the previously discussed structure, to excite the fundamental TE mode, and the center-to-center spacing between waveguides is again 50 ¯m. In this structure, the bend radius of each waveguide starts near 26 mm and decreases by 2 mm with each round trip. After three round trips, an s-bend of 9.8 mm bend radius is used to change direction and spiral outward in another three round trips back to the initial bend radius of 26 mm. One should note that the OFDR loss measurement is independent of the fiber-to-chip coupling. When measuring small total propagation loss, OFDR is therefore more accurate than the commonly used cut-back measurement technique, which has an error term associated with the uncertainty in fiber-to-chip coupling loss.
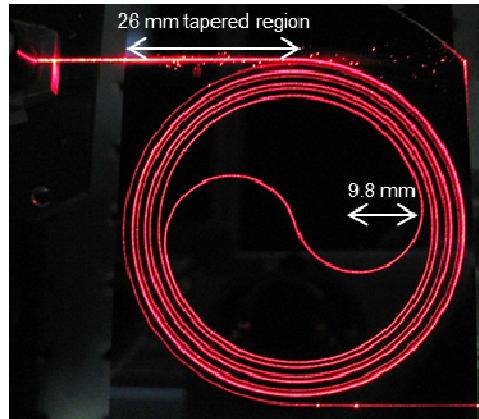

Fig. 7. Red laser light propagating in a 1.032 meter spiral delay with PECVD upper cladding.

Figure 8 shows the spectral dependence of the propagation loss in a waveguide with a 50-nm-thick by 6.5-¯m-wide core and PECVD oxide upper cladding. A 10 nm window is used to filter the data in the spectral domain before a fit to Eq. (9). Using Eqs. (4) and (9), the spectral window width can be reduced to around 1 pm before the uncertainty in group index gives an uncertainty in $\alpha_1^{dB/m}$ on the same order as $\alpha_1^{dB/m}$. The larger window width is required to increase the number of data points in the fit and reduce fitting error due to the physical deviation in the backscatter amplitude, which dominates the total measurement error. The window is moved in increments of 100 pm in order to extract the spectral dependence of the propagation loss.

The smaller central axes in Fig. 8 show the "big picture" of how propagation loss depends on the location of several absorption loss peaks, fit here by Gaussian functions, and interfacial scattering loss. Because of the spectral window width, some averaging of the actual scattering and absorption features is expected. The color key in Fig. 8 gives the central wavelengths of the various Gaussian fits to the data. The fundamental absorptions of these overtone peaks are

commonly measured using Fourier transform infrared spectroscopy [15]. From such measurements, absorption losses around 1.3-1.4 µm are commonly attributed to OH impurities, while those around 1.52 and 1.55-1.57 µm are attributed to N-H and Si-H impurities, respectively. No data are obtained in the 1.35-1.52 µm wavelength regime, and so no absorption peaks can be fit there. Though the scattering loss fit extends through this regime, it should be treated only as an estimated propagation loss limit for the waveguide at those wavelengths.

The upper-left axes of Fig. 8 show the loss measured with OFDR over a wavelength range of 1.28 to 1.33 µm. In this regime, the loss can be described as the sum of loss due to OH absorption and interfacial scattering losses. The minimum total loss measured for the waveguide in this regime is (0.45 ± 0.1) dB/m near a wavelength of 1.29 µm. The upper-right axes show the loss measured with OFDR over a wavelength range of 1.53 to 1.605 µm. Here, loss can be described as the sum of N-H absorption, Si-H absorption, and scattering loss contributions. The minimum total propagation loss in this regime, obtained for the longest measurement wavelengths that are furthest away from the absorption peaks, is (0.05 ± 0.1) dB/m.
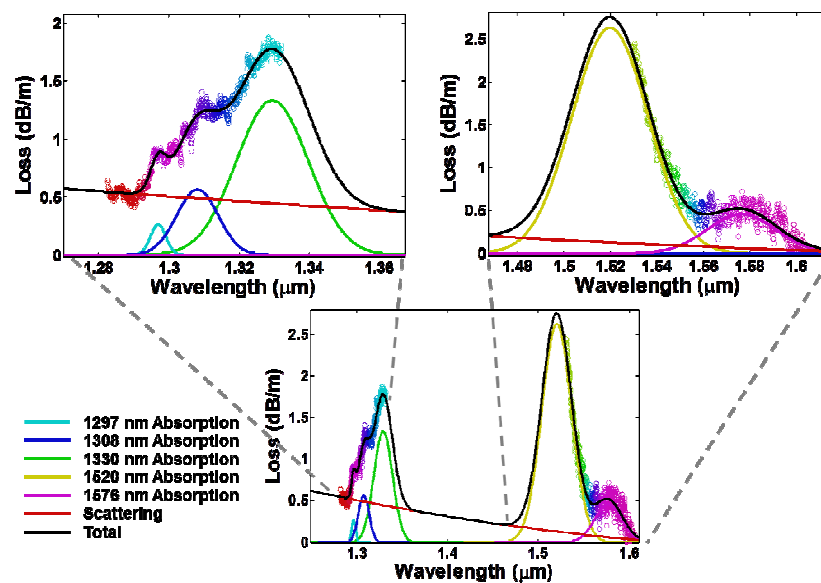

Fig. 8. Total propagation loss (circles) vs. wavelength for a 50-nm-thick by 6.5-µm-wide waveguide with PECVD oxide upper cladding. A 10 nm window function is applied in the spectral domain. The solid lines are fits of Gaussians (absorption loss) and a polynomial (scattering loss) to the data. The color key gives the loss type colors and the center wavelengths of the various Gaussian fits. The color of each data marker is a linear combination of the loss type colors that contribute to it. Due to spectral averaging, the Gaussian fits are broader and have lower peaks than the actual spectral dependence of propagation loss.

Figure 9 shows the propagation loss in a waveguide with a 40-nm-thick by 13-µm-wide core and bonded thermal oxide upper cladding. Since the loss is lower, a 50 nm spectral window is applied to data from this waveguide in order to reduce the measurement uncertainty. The lower axes again show the location of common absorption peaks measured in dielectric films along with wavelength dependent scattering loss. The upper-left axes show propagation loss measured over the wavelength range centered near 1.3 µm. The minimum total propagation loss in this regime is (0.33 ± 0.03) dB/m, however, the loss is relatively flat over the entire spectral regime. This indicates a decrease or shift in the OH absorption peak observed for the waveguides with PECVD upper cladding. The upper-right axes show propagation loss measured over the wavelength range centered near 1.57 µm. Though the loss can again be resolved into N-H absorption, Si-H absorption, and scattering loss contributions,

the loss at shorter wavelengths is reduced by about 0.5 dB/m. This suggests that the absorption loss in this regime may have also been decreased. The minimum total propagation loss in this regime, (0.045 ± 0.04) dB/m, is again obtained at the longest measurement wavelengths, which are furthest away from the absorption peaks.
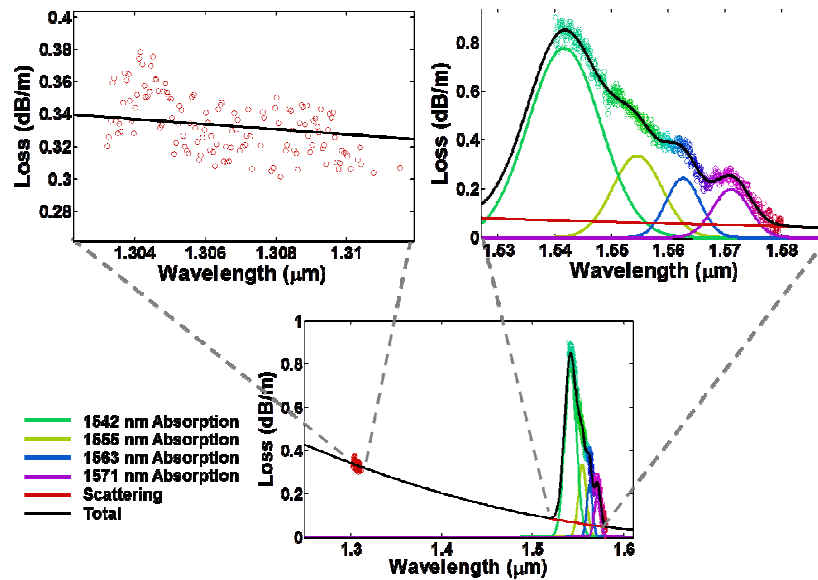

Fig. 9. Total propagation loss (circles) vs. wavelength for a 40-nm-thick by 13-¯m-wide waveguide with bonded thermal oxide upper cladding. A 50 nm window function is applied in the spectral domain. The solid lines are fits of Gaussians (absorption loss) and a polynomial (scattering loss) to the data. The color key gives the loss type colors and the center wavelengths of the various Gaussian fits. The color of each data marker is a linear combination of the loss type colors that contribute to it. Due to spectral averaging, the Gaussian fits are broader and have lower peaks than the actual spectral dependence of propagation loss.

4. Conclusions

We have demonstrated silica-based planar waveguides with record low propagation loss of (0.045 ± 0.04) dB/m in the 1580-1610 nm wavelength regime. The waveguides have a high-aspect-ratio stoichiometric Si_3N_4 core and a large mode area that helps reduce scattering loss at the core-cladding interfaces. The loss is highly wavelength dependent due to hydrogen impurities in the dielectric films, but these absorption losses can be at least partially mitigated through the bonding of thermally grown oxide upper cladding. Since the growth of thermal oxide and the waveguide processing may take place in parallel, waveguides with bonded thermal oxide upper claddings have shorter fabrication times. Data also suggest that the dielectric films in waveguides with bonded thermal upper claddings have lower residual stress than those fabricated with PECVD oxide.

Acknowledgements